Eulerian Simulations of Local Liquid Distribution in a Trickle Bed : Effect of Flow Rates and Liquid Properties

Rohit Gulia, D. Saxena, Y. Haroun, F. Augier, Vivek Buwa

To cite this version:

Rohit Gulia, D. Saxena, Y. Haroun, F. Augier, Vivek Buwa. Eulerian Simulations of Local Liquid Distribution in a Trickle Bed : Effect of Flow Rates and Liquid Properties. Chemical Engineering Science, 2023, 282, pp.119212. 10.1016/j.ces.2023.119212 . hal-04452151

HAL Id: hal-04452151
https://ifp.hal.science/hal-04452151v1

Submitted on 12 Feb 2024

Eulerian Simulations of Local Liquid Distribution in a Trickle Bed: Effect of Flow rates and Liquid Properties

Rohit S. Gulia[1], D. Saxena[1], Y. Haroun[2], F. Augier[2], Vivek V. Buwa[1, *]
[1] Department of Chemical Engineering, Indian Institute of Technology, Delhi, New Delhi 110016, India
[2] IFP Energies Nouvelles, Rond-point de l'échangeur de Solaize, BP 3, 69360 Solaize, France
*Corresponding author: (Tel: +91 11 2659 1027, email: vvbuwa@iitd.ac.in)

Abstract

Trickle Bed Reactors (TBRs) are widely used for production of cleaner fuels. For a given catalyst and process conditions, the performance of TBRs is known to be influenced by the local liquid volume fraction (ε_L) distribution. In the present work, we performed Eulerian multi-fluid simulations to understand the contributions of different interphase interaction forces such as gas-liquid ($\vec{\mathrm{F}}_{\mathrm{GL}}$), gas-solid ($\vec{\mathrm{F}}_{\mathrm{GS}}$) and liquid-solid ($\vec{\mathrm{F}}_{\mathrm{LS}}$) forces, capillary pressure force ($\vec{\mathrm{F}}_{\mathrm{C}}$) and mechanical dispersion force ($\vec{\mathrm{F}}_{\mathrm{D}}$) to the local liquid spreading and how their contributions change with changes in gas and liquid flow rates (Q_G and Q_L), surface tension (σ) and liquid viscosity (μ_L). Further, we also simulated the effects of Q_G, Q_L, σ and μ_L on bed scale parameters such as pressure drop (ΔP) and overall liquid hold-up ($\langle\varepsilon_L\rangle$) and importantly on the local liquid spreading and validated the predictions using the measurements. Using the simulations performed for different particle diameters without and with $\vec{\mathrm{F}}_{\mathrm{C}}$ and $\vec{\mathrm{F}}_{\mathrm{D}}$, we show that the $\vec{\mathrm{F}}_{\mathrm{D}}$ contributes marginally to the local liquid spreading. Through the comparison of the order of magnitudes of $\vec{\mathrm{F}}_{\mathrm{GL}}$, $\vec{\mathrm{F}}_{\mathrm{GS}}$ and $\vec{\mathrm{F}}_{\mathrm{LS}}$, we show that $\vec{\mathrm{F}}_{\mathrm{LS,y}}$ significantly contributes to local liquid spreading, ΔP and $\langle\varepsilon_L\rangle$. While the use of existing $\vec{\mathrm{F}}_{\mathrm{LS}}$ model proposed by Boyer et al. (2007) was found to overpredict the local liquid spreading, ΔP and $\langle\varepsilon_L\rangle$, the modified $\vec{\mathrm{F}}_{\mathrm{LS}}$ model led to satisfactory predictions of ΔP and $\langle\varepsilon_L\rangle$. The predictions of the local liquid spreading, ΔP and $\langle\varepsilon_L\rangle$ are validated using the measurements of Saxena et al. (2023) for different Q_G, Q_L, σ and μ_L and the modified model was found to accurately predict the local liquid spreading, ΔP and $\langle\varepsilon_L\rangle$ for wide range of parameters. Further, despite the increase in liquid accumulation in centre due to increase in the gradient of ε_L and $\vec{\mathrm{F}}_{\mathrm{C}}$, the lateral liquid spreading is found to marginally decrease with the decrease in σ. We also found the contribution of viscous components of $\vec{\mathrm{F}}_{\mathrm{GL}}$, $\vec{\mathrm{F}}_{\mathrm{GS}}$ and $\vec{\mathrm{F}}_{\mathrm{LS}}$ to the lateral liquid spreading to be negligible. However, a significant increase in ε_L and ΔP with the increase in μ_L was observed. The present work is an important step in extending the experimentally validated CFD model for reactor simulations by incorporating reactions and heat effects.

Keywords: Trickle-bed reactor, Local liquid distribution, Computational Fluid Dynamics, surface tension, viscosity, Eulerian simulations.

1 Introduction

Trickle bed reactors (TBRs) are widely used for hydro-desulfurization and hydrocracking of petroleum products and the hydrogenation of vegetable oils. Due to rising environmental concerns and strict restrictions (e.g., sulphur content < 10 ppm) on fuel quality, it has become essential to improve the performance of TBRs. For a given catalyst and process conditions, the performance of TBRs is strongly influenced by the local liquid distribution. A poor liquid distribution can result in localised hot spots (e. g., Agrawal et al., 2007; Atta et al., 2007). The local liquid distribution inside a TBR is a strong function of fluid flow rates, particle shape/size, and fluid physical properties such as surface tension (σ) and liquid viscosity (μ_L). Therefore, it is important to develop computational fluid dynamics (CFD) models that can accurately predict the local liquid distribution in TBRs.

Since the pressure drop across the bed (ΔP) and the overall liquid holdup ($\langle\varepsilon_L\rangle$) are the key hydrodynamic parameters, significant research efforts have been made to develop CFD models that can accurately predict the ΔP and $\langle\varepsilon_L\rangle$. Over the last few decades, the effects of the parameters like fluid flow rates and wettability on ΔP and $\langle\varepsilon_L\rangle$ have been extensively studied (Al-Dahhan et al., 1998; Jiang et al., 2002; Gunjal et al., 2003, 2005; Boyer et al., 2007 and Lappalainen et al., 2009). Moreover, a few studies in the past emphasised the importance of hydraulic tortuosity (the flow path of a liquid phase in a tortuous structure) in porous media (Narasimhan et al., 2004; Boyer et al., 2007; Ghanbarian et al., 2013) to improve the predictions of ΔP and $\langle\varepsilon_L\rangle$. Ghanbarian et al. (2013) recommended the inclusion of the tortuosity (hydraulic) factor in the gas-liquid ($\vec{\mathrm{F}}_{\mathrm{GL}}$), gas-solid ($\vec{\mathrm{F}}_{\mathrm{GS}}$) and liquid-solid ($\vec{\mathrm{F}}_{\mathrm{LS}}$) interphase interaction force closure models proposed by Attou and Ferschneider (1999, 2000) in order to use these models for the flow through the complex/tortuous structures. Narasimhan et al. (2004)

reported that the tortuous paths and the tortuosity effects change with flow parameters. Later, Boyer et al. (2007) modified the $\vec{\mathrm{F}}_{\mathrm{LS}}$ proposed by Attou and Ferschneider (1999) to including the liquid flow tortuosity factor, to improve the predictions of ΔP and $\langle \varepsilon_L \rangle$. However, the modification proposed by Boyer et al. (2007) in the $\vec{\mathrm{F}}_{\mathrm{LS}}$ closure model depends on the nature of the fluids (i.e., aqueous, or organic fluids). However, a CFD model that can not only predict the ΔP and $\langle \varepsilon_L \rangle$ accurately over a wide range of parameters like fluid flow rates and fluid physical properties (e.g., σ and μ_L) but also the local liquid distribution continues to be a challenge.

In the past, the Eulerian multi-fluid model has been used to simulate the bed-scale local liquid distribution in TBRs, in which the volume-averaged mass and momentum conservation equations are solved for both the fluid phases (i.e., gas and liquid), whereas the solid phase remains stationary (e.g., see Jindal and Buwa, 2017; Dhanraj and Buwa, 2018; Boyer et al., 2005; Jiang et al., 2002). Since the Eulerian multi-fluid model assumes all the phases to be in interpenetrating continuum, different closure models have been proposed to calculate the momentum exchange through the gas-liquid ($\vec{F}_{GL}$), gas-solid ($\vec{F}_{GS}$) and liquid-solid ($\vec{F}_{LS}$) interaction forces (Saez and Carbonell, 1985; Holub et al., 1992; Attou and Ferschneider, 1999), mechanical dispersion ($\vec{F}_D$) (Lappalainen et al., 2011, 2009a), and capillary pressure force ($\vec{F}_C$) (Attou and Ferschneider, 1999a; Lappalainen et al., 2009b). In the past, $\vec{F}_C$ was calculated in two different ways, i.e., $\vec{F}_C = \varepsilon_L \nabla P_C$ (e.g., Solomenko et al., 2015; Lappalainen et al., 2009b), and $\vec{F}_C = -P_C \nabla \varepsilon_L$ (Boyer et al., 2005; Jiang et al., 2002; Jindal and Buwa, 2017; Dhanraj and Buwa, 2018). $\vec{F}_C = \varepsilon_L \nabla P_C$ formulation leads to an additional factor $\varepsilon_L/3(1 - \varepsilon_G)$ in the original mechanistic model proposed by Attou and Ferschneider (1999), which diminishes the effect of the d_P, Q_G and Q_L on the local liquid spreading (Dhanraj and Buwa, 2018).

Furthermore, the mechanical dispersion force ($\vec{\mathrm{F}}_{\mathrm{D}}$) is also known to affect the liquid distribution inside TBRs (Lappalainen et al., 2011, 2009a). Typically, in TBRs, the $\vec{\mathrm{F}}_{\mathrm{D}}$ arises (a) due to the velocity gradients because of the presence of solid particle walls, (b) due to the variation in the pore size, and (c) due to fluctuations in mean flow streamlines (Lappalainen et al., 2009b). A few researchers have discussed the phenomenological model for $\vec{\mathrm{F}}_{\mathrm{D}}$ (Lappalainen et al., 2009a, 2011; Fourati et al., 2013). Lappalainen et al. (2009a) investigated the contribution of $\vec{\mathrm{F}}_{\mathrm{D}}$ to the liquid spreading and showed that the $\vec{\mathrm{F}}_{\mathrm{D}}$ has a significant effect on lateral liquid spreading at large $\mathrm{d_P}$ (approx. $\mathrm{d_P} > 10$ mm). Further, Solomenko et al. (2015) reported that it is important to incorporate the closure model of $\vec{\mathrm{F}}_{\mathrm{D}}$ for both gas and liquid phases to capture the desired lateral liquid spreading and showed that the contribution of $\vec{\mathrm{F}}_{\mathrm{D}}$ is significant for the spherical particles with $\mathrm{d_P} \geq 6$ mm. However, Jindal and Buwa (2017) and Dhanraj and Buwa (2018) showed that the capillary pressure formulation of $\vec{\mathrm{F}}_{\mathrm{C}} = -\,\mathrm{P_C}\nabla$ is sufficient to predict the local liquid distribution for $d_P \leq 8$ mm. Due to these uncertainties, the necessity of $\vec{\mathrm{F}}_{\mathrm{D}}$ for the predictions of local liquid distribution in TBRs packed with spherical particles needs to be further investigated.

In the past contributions from our research group (e.g., see Solomenko et al., 2015 and Jindal and Buwa, 2017), investigations on the effect of $\mathrm{Q_G}$, $\mathrm{Q_L}$ and $\mathrm{d_P}$ on the liquid spreading using two different approaches (i.e., porous media and Eulerian) are reported. According to Solomenko et al. (2015), an increase in $\mathrm{Q_L}$ promotes radial liquid spreading only close to the bed inlet, whereas $\mathrm{Q_G}$ has a negligible effect on the radial liquid spreading. However, it is still not known whether the model can accurately predict the observed change in the radial liquid spreading in the measurements with the change in $\mathrm{Q_L}$, because of the limited range of operating conditions considered in the previous work. Later, Jindal and Buwa (2017) showed an increase in lateral liquid spreading with the increase in Q_L, whereas the model was comparatively less sensitive towards the change in the lateral liquid spreading with the change in Q_G as compared to the observed change in the lateral liquid spreading. Since the model was found to overpredict the effect of Q_G, Q_L and d_P, an empirical modification to the $\vec{F}_C$ was proposed to accurately predict the effect of the parameters mentioned above on the local liquid spreading. While the modified model accurately predicted the effect of d_P on the dynamics of liquid spreading, the ability of the model to predict the effects of Q_G, Q_L, σ and μ on the local liquid spreading, ΔP and $\langle \varepsilon_L \rangle$ are still needs to be established.

In order to predict the effects of Q_G, Q_L, σ and μ_L on the local liquid spreading, ΔP and $\langle \varepsilon_L \rangle$; it is important understand how the order of magnitude of different interphase coupling forces ($\vec{F}_{GL}$, $\vec{F}_{GS}$ and $\vec{F}_{LS}$) change with the change in Q_G, Q_L, σ and μ_L and influence the local liquid distribution. Further, how the particle diameter influences contributions of the capillary and mechanical dispersion forces, that govern the lateral (or radial) liquid spreading, was investigated in past by the Solomenko et al. (2015), David and Buwa (2018) and Lappalainen et al. (2009b). However, how these forces scale with Q_G, Q_L, σ and μ_L and influence the local liquid spreading is not yet understood.

Further, it is important to develop a CFD model that can not only predict the effects of Q_G, Q_L and d_P on the liquid distribution but also can predict the effects of the fluid phase properties (σ and μ_L) on the local liquid distribution. Moreover, as discussed before it is also important to understand how the contributions of different interphase coupling forces, capillary and mechanical dispersion forces vary with Q_G, Q_L, σ and μ_L; and their influence on the local liquid distribution in TBRs at different operating conditions. It is also important to validate the predictions of the CFD models using local liquid distribution measurements under different operating conditions. In view of this, the present work is carried out with following objectives (a) to investigate the effects of Q_G, Q_L, σ and μ_L on the local liquid distribution, ΔP and $\langle \varepsilon_L \rangle$, (b) to experimentally validate the CFD model at different Q_G, Q_L, σ and μ_L, (c) to understand the contributions of interphase coupling forces, capillary and mechanical dispersion forces to the liquid spreading at different Q_G, Q_L, σ and μ_L.

2 Computational Model

2.1 Governing equations

The Eulerian multi-fluid model, which assumes the fluid phases to be in interpenetrating continuum, is used to simulate gas-liquid flow in a pseudo-2D rectangular bed as considered in the measurements. The volume-averaged continuity and momentum equations are solved for each fluid phase (air and water), whereas the solid phase remains stationary. The conservation equations for fluid phases by assuming the flow to be laminar and fluids to be incompressible and Newtonian are given as follows:

Gas phase:

$$\frac{\partial}{\partial t}(\varepsilon_G \rho_G) + \nabla \cdot (\varepsilon_G \rho_G \vec{u}_G) = 0 \tag{1}$$

$$\frac{\partial}{\partial t}(\varepsilon_G \rho_G \vec{u}_G) + \nabla \cdot (\varepsilon_G \rho_G \vec{u}_G \vec{u}_G) = -\varepsilon_G \nabla P + \nabla \cdot (\varepsilon_G \mu_G \nabla \vec{u}_G) + \varepsilon_G \rho_G \vec{g} + \vec{F}_{GL} + \vec{F}_{GS} + \vec{F}_{D,G} \tag{2}$$

Liquid phase:

$$\frac{\partial}{\partial t}(\varepsilon_L \rho_L) + \nabla \cdot (\varepsilon_L \rho_L \vec{u}_L) = 0 \tag{3}$$

$$\frac{\partial}{\partial t}(\varepsilon_L \rho_L \vec{u}_L) + \nabla \cdot (\varepsilon_L \rho_L \vec{u}_L \vec{u}_L) = -\varepsilon_L \nabla P + \nabla \cdot (\varepsilon_L \mu_L \nabla \vec{u}_L) + \varepsilon_L \rho_L \vec{g} + \vec{F}_{LG} + \vec{F}_{LS} + \vec{F}_C + \vec{F}_{D,L} \tag{4}$$

In **Eqs. (1) - (4)**, ε_L and ε_G represent the liquid- and gas- phase volume fractions, respectively. ρ_L and ρ_G are the liquid- and gas- phase densities, μ_L and μ_G are liquid- and gas-phase viscosities, respectively, and $\vec{u}_L$ and $\vec{u}_G$ represent the liquid- and gas- phase velocities, respectively. $\vec{F}_{LS}$, $\vec{F}_{GL}$ and $\vec{F}_{GS}$ account for the momentum exchange between liquid and solid, gas and liquid-, gas- and solid- phases, respectively. $\vec{F}_C$ accounts for the capillary pressure force that arises due to the pressure difference across the interface between two immiscible phases (liquid- and gas-). $\vec{\mathrm{F}}_{\mathrm{DL}}$ and $\vec{\mathrm{F}}_{\mathrm{DG}}$ represents the mechanical dispersion forces for the liquid- and gas- phases, respectively.

Phase interaction forces:

The phenomenological models for phase interaction forces and capillary pressure given by Attou and Ferschneider (1999) and Attou and Ferschneider (2000) are used in the present work.

$$\vec{F}_{GL} = K_{GL}\,(\vec{u}_G - \vec{u}_L) \tag{5}$$

$$\vec{F}_{GS} = K_{GS}\,(\vec{u}_G) \tag{6}$$

$$\vec{F}_{LS} = K_{LS}\,(\vec{u}_L) \tag{7}$$

Where, $\mathrm{K}_{\mathrm{GL}}, \mathrm{K}_{\mathrm{GS}}$ and K_{LS} are the gas-liquid, gas-solid and liquid-solid interphase interaction coefficients [see **Eqs (5) – (7)**], and are calculated as shown below in **Eqs. [(8)-(10)]**.

$$K_{GL} = \varepsilon_G \left(\underbrace{\frac{E_1 \mu_G (1-\varepsilon_G)^2}{{d_P}^2 {\varepsilon_G}^2} \left(\frac{\varepsilon_S}{1-\varepsilon_G} \right)^{\frac{2}{3}}}_{\text{Viscous (v-component)}} + \underbrace{\frac{E_2 \rho_G (1-\varepsilon_G)}{d_P \varepsilon_G} \left(\frac{\varepsilon_S}{1-\varepsilon_G} \right)^{\frac{1}{3}} |\vec{u}_G - \vec{u}_L|}_{\text{Inertial (i-component)}} \right) \tag{8}$$

$$K_{GS} = \varepsilon_G \left(\underbrace{\frac{E_1 \mu_G (1-\varepsilon_G)^2}{{d_P}^2 {\varepsilon_G}^2} \left(\frac{\varepsilon_S}{1-\varepsilon_G} \right)^{\frac{2}{3}}}_{\text{Viscous (v-component)}} + \underbrace{\frac{E_2 \rho_G (1-\varepsilon_G)}{d_P \varepsilon_G} \left(\frac{\varepsilon_S}{1-\varepsilon_G} \right)^{\frac{1}{3}} |\vec{u}_G|}_{\text{Inertial (i-component)}} \right) \tag{9}$$

$$K_{LS} = \varepsilon_L \left(\underbrace{\frac{E_1 \mu_L {\varepsilon_S}^2}{{d_P}^2 {\varepsilon_L}^2}}_{\substack{\text{Viscous} \\ \text{(v-component)}}} + \underbrace{\frac{E_2 \rho_L \varepsilon_S}{d_P \varepsilon_L} |\vec{u}_L|}_{\substack{\text{Inertial} \\ \text{(i-component)}}} \right) \tag{10}$$

In **Eqs. (8) – (10)**, E_1 and E_2 are the Ergun constants; the values for these constants used in the present work are 180 and 1.8, respectively (Jindal and Buwa, 2017). ε_{S} and d_{P} represent the solid phase volume fraction and particle diameter, respectively.

Further, the capillary pressure force formulation proposed by Attou and Ferschneider (2000) and further modified by Dhanraj and Buwa (2018) is used in the present work for the calculation of $\vec{\mathrm{F}}_{\mathrm{C}}$:

$$\vec{F}_C = -P_c \nabla \varepsilon_L = -2\sigma \left(\frac{\varepsilon_S}{1-\varepsilon_G}\right)^{\frac{1}{3}} \left(\frac{1}{(1-\varepsilon_S)d_p}\right) \left(1 + 88.1\frac{\rho_G}{\rho_L}\right) \left[\frac{d_p}{d_{thr}}({\varepsilon_S}^{0.6})\right]^{-13.957} \nabla \varepsilon_L \tag{11}$$

where, the capillary pressure ($\mathrm{P_c}$) is:

$$P_C = -2\sigma \left(\frac{\varepsilon_S}{1-\varepsilon_G}\right)^{\frac{1}{3}} \left(\frac{1}{(1-\varepsilon_S)d_p}\right) \left(1 + 88.1\frac{\rho_G}{\rho_L}\right) \left[\frac{d_p}{d_{thr}}({\varepsilon_S}^{0.6})\right]^{-13.957} \tag{12}$$

In **Eq. (12),** σ is the air-water surface tension, and d_{thr} is the throat diameter which is calculated by dividing the total bed pore volume ($\sum_i V_i$) by the total surface area of bed pores ($\sum_i SA_i$) as shown below in **Eq. (13)**.

$$d_{thr} = 6\left(\frac{\frac{\sum_i V_i}{N}}{\frac{\sum_i SA_i}{N}}\right) = 6\left(\frac{(1-\varepsilon_S)V_B}{\left(\frac{V_B \varepsilon_S}{V_P}\right)\pi d_p^2}\right) = \left(\frac{1-\varepsilon_S}{\varepsilon_S}\right) d_p \tag{13}$$

In **Eq. (13),** V_B, V_P, and N are the bed volume, the volume of a particle, and the number of pores, respectively.

Mechanical dispersion forces:

The mechanical dispersion force closure model proposed by Lappalainen et al. (2009b and 2011) is used in the present work.

$$\vec{F}_{D,G} = K_{GL}\vec{u}_{D,G} + K_{GL}(\vec{u}_{D,G} - \vec{u}_{D,L}) \tag{14}$$

$$\vec{F}_{D,L} = K_{LS}\vec{u}_{D,L} + K_{GL}(\vec{u}_{D,L} - \vec{u}_{D,G}) \tag{15}$$

In **Eqs. (14) and (15)**, $\vec{u}_{D,G}$, $\vec{u}_{D,L}$ and are the drift velocities for the gas and liquid phase, respectively, and are calculated as:

$$\vec{u}_{D,\mathrm{i}} = -\frac{S_m}{\varepsilon_k}\left[\|\vec{u}_k\|\nabla\varepsilon_\mathrm{i} - (\vec{u}_\mathrm{i}\cdot\nabla\varepsilon_\mathrm{i})\frac{\vec{u}_\mathrm{i}}{\|\vec{u}_\mathrm{i}\|}\right] \tag{16}$$

In **Eq. 16** $\mathrm{S_m}$ is the spread factor, which is calculated by the correlation proposed by Lappalainen et al. (2009b) as shown below:

$$S_m = 0.015 \times {d_P}^{0.5} \tag{17}$$

2.2 Solution domain, boundary conditions, and numerics

The solution domain, the same as that used for measurements, is considered for the simulations (see **Figure 1).** Air ($\rho_\mathrm{G} = 1.225\ \mathrm{kg/m^3}, \mu_\mathrm{G} = 1.789 \times 10^{-5}\ \mathrm{kg/ms}$) is used as the primary phase, water ($\rho_\mathrm{L} = 998.2\ \mathrm{kg/m^3}, \mu_\mathrm{G} = 0.001\ \mathrm{kg/ms}$) and glass ($\mathrm{d_P} = 2 - 8\ \mathrm{mm}, \rho_\mathrm{S} = 2500\ \mathrm{kg/m^3}$) are used as the secondary phases. The average bed porosity measured by Saxena et al. (2023) is considered in the present work, and all the simulations are performed by patching liquid volume faction of 0.01 to mimic the pre-wetting condition in the complete domain. The velocity inlet boundary condition is specified at the gas and liquid inlets, and the no-slip condition is specified at column walls. The pressure outlet boundary condition with zero-gauge pressure is specified at the outlet.

The commercial flow solver ANSYS FLUENT 2021R1 is used to perform transient 3D simulations on a pseudo-2D rectangular column using the Semi-Implicit Method for Pressure Linked Equations (SIMPLE) algorithm for pressure-velocity coupling. Quadratic Upstream Interpolation for Convective Kinematics (QUICK) scheme is used to discretise spatial derivatives. The first-order implicit scheme is used to discretise the time derivatives [**Eqs. (1) – (4)**]. The interphase interaction forces, capillary pressure, and mechanical dispersion forces [**Eqs. (5) – (17)**] are implemented in the commercial solver using the user-defined functions (UDFs). All the simulations reported in present work were performed using the PADUM: Hybrid High-Performance Computing (HPC) facility at the Indian institute of technology (IIT), Delhi. The typical computational time needed for simulations to reach steady-state varies between 40 to 120 hours on an 8-core processor.

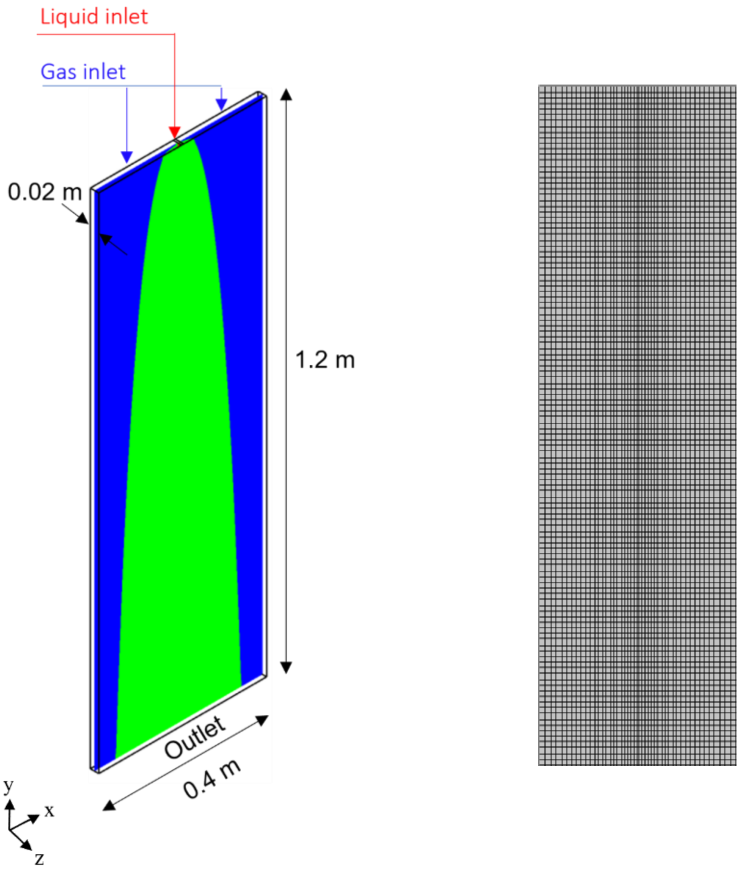

Geometry Mesh

Figure 1. Typical computational domain and mesh

3 Experiments

The local liquid spreading measurements were performed using high speed imaging in our research group by Saxena et al. (2023) using a pseudo-2D rectangular column (H = 1.2 m, W = 0.4 m, D = 0.02 m) packed with spherical glass beads ($d_P = 0.004\ m$) were used to validate the simulations reported in present work. The details of the measurements performed for the Q_G and Q_L in the range of 0 - 10 Nm^3/h and 0.024 – 0.054 m^3/h, respectively, and for the three different values of σ (0.025, 0.052 and 0.072 N/m) and μ_L (0.001, 0.005 and 0.01 Pa·s) used in the present work can be found in Saxena et al. (2023). During all these measurements the system was allowed to achieve the steady state liquid spreading. The measured steady-state liquid distribution, bed pressure drop (ΔP), and overall liquid holdup ($\langle\varepsilon_L\rangle$) for the above-mentioned Q_G, Q_L, σ and μ_L were used in the present work to validate the CFD model.

4 Results and discussion

The initial simulations were performed to investigate the effect of grid resolution on the steady-state liquid distribution, ΔP/L (L is the length of column) and $\langle\Delta\varepsilon_L\rangle$. Simulations were performed until the lateral liquid spreading, ΔP and $\langle\Delta\varepsilon_L\rangle$ were found to be constant (indicating steady state). Three different grids, coarse (12000 cells with Δx = 0.008 m, Δy = 0.01 m, Δz = 0.01 m), medium (24000 cells with Δx = 0.008 m, Δy = 0.01 m, Δz = 0.005 m) and fine (48000 cells with Δx = 0.005 m, Δy = 0.01 m, Δz = 0.004 m) were considered. The steady-state liquid distribution and liquid fronts for these three grids are shown in **Figure 2 [(a) - (d)].** The steady state liquid front lines shown in **Figure 2 [(a) - (d)]** and in all subsequent figures are the isolines of ε_L on center plane i.e., z = 0.01 m, extracted at the 7 % of bed porosity (i.e., isolines at ε_L = 0.07ε). Qualitatively, the effect of grid resolution on the steady-state liquid distribution was found to be marginal for the medium and fine grids (see **Figure 2**).

Table 1: Effect of grid size on pressure drop and overall liquid volume fraction

Grid	Pressure drop (ΔP/L, N/m^3)	Overall liquid volume fraction $\langle\Delta\varepsilon_L\rangle$
Coarse (12000)	380	0.0309
Medium (24000)	464	0.0311
Fine (48000)	490	0.0313

The effect of grid size on the ΔP/L and the $\langle\Delta\varepsilon_L\rangle$ is shown in **Table 1**. The change in the pressure drop predicted using coarse and fine grid was 22.45 % and that between medium and fine grid was 5.3 %. The change in the overall liquid volume fraction for all the three grid sizes was found to be less than 1 %. Therefore, all further simulations were performed by using the medium grid.

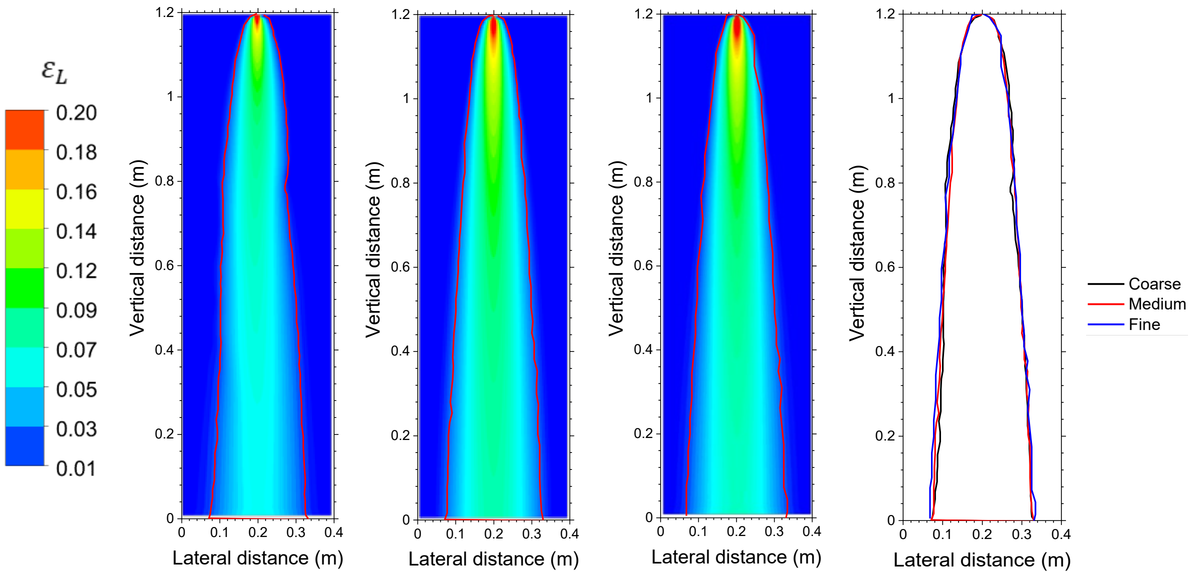

(a) (b) (c) (d)

Figure 2. Effect of grid resolution on the steady-state liquid distribution for three different grid sizes (a) coarse (12,000 cells), (b) medium (24,000 cells), (c) fine (48,000 cells), and (d) comparison of steady-state liquid fronts for different grids ($Q_L = 0.054$ m^3/h, $Q_G = 6$ Nm^3/h, $d_P = 0.004$ m)

4.1 Forces governing bed scale liquid spreading in TBR

As mentioned in Section 1, the capillary pressure, interphase interaction and mechanical dispersion forces govern the bed-scale liquid spreading. Capillary pressure (P_c) arises due to the pressure difference across the interface between the two fluids. The interphase interaction terms $\vec{F}_{GL}$, $\vec{F}_{GS}$, and $\vec{F}_{LS}$ represent the momentum exchange between gas-liquid, gas-solid, and liquid-solid phases, respectively. To understand the relative contributions of different forces, we compared the x-, y- and z- components of different forces in the entire solution domain at steady-state conditions. The histograms of different components of forces at steady state shows that only the y-component (axial) of $\vec{F}_{GL,}$, $\vec{F}_{GS}$ and $\vec{F}_{LS}$ terms and the x-component (lateral) of $\vec{F}_C$, $\vec{F}_{D,\,G}$ and $\vec{F}_{D,\,L}$ are dominant **(Supplementary Figure 1, 2 and 3 (a)).** Therefore, only these components of the respective forces are analyzed in this and all subsequent sections. As mentioned in Section 1, different capillary pressure formulations ($-P_c\nabla\varepsilon_L$ and $\varepsilon_L\nabla P_c$) were used in past to simulate the bed-scale liquid distribution. While $-P_c\nabla\varepsilon_L$ was found to overpredict the liquid spreading (Jindal and Buwa, 2018), the $\varepsilon_L \nabla P_c$ formulation required additional closure models of the mechanical dispersion forces ($\vec{F}_{D,G}$ and $\vec{F}_{D,L}$) to predict the liquid distribution (Solomenko et al., 2015). Due to these uncertainties, the effect of order of magnitude of $\vec{F}_{D,G}$ and $\vec{F}_{D,L}$ on the liquid distribution at bed scale was further investigated.

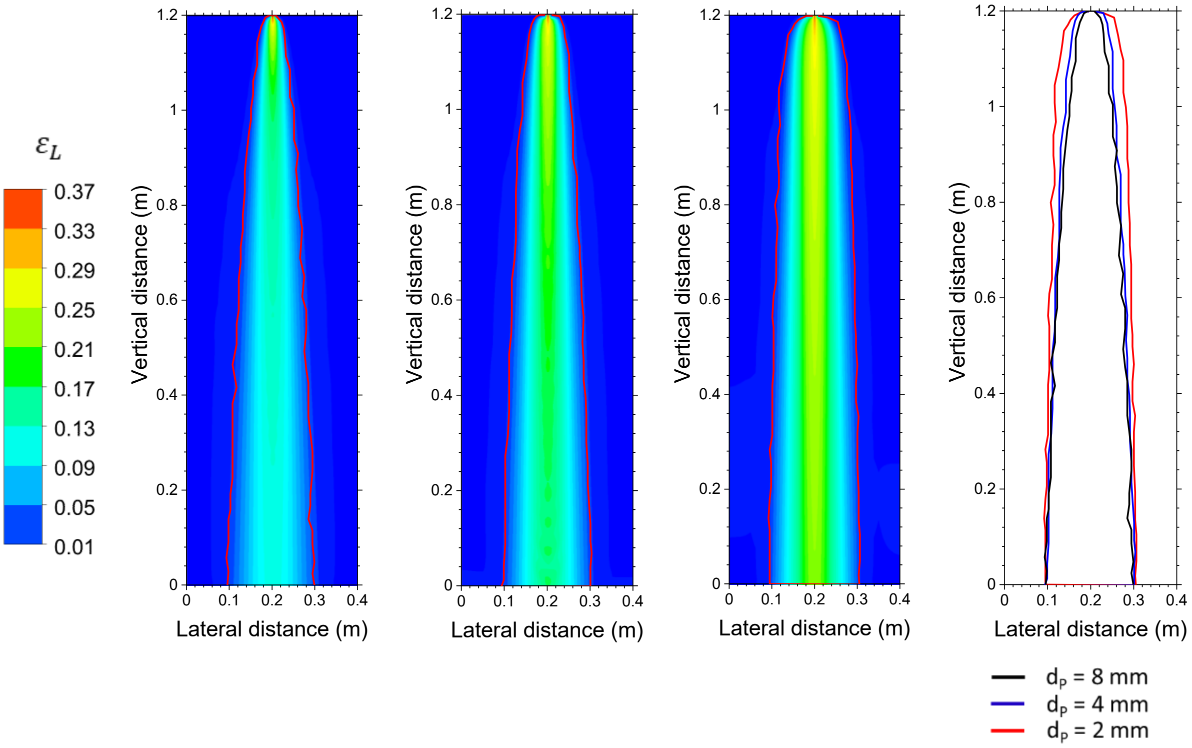

(a) (b) (c) (d)

Figure 3. Effect of particle diameter on the liquid volume fraction distribution, (a) 8, (b) 4, and (c) 2 mm, and (d) comparison of the steady-state liquid fronts ($Q_L = 0.054$ m^3/h, $Q_G = 6$ Nm^3/h)

To understand the contribution of $\vec{F}_{D,G}$ and $\vec{F}_{D,L}$ to the bed-scale liquid distribution, we performed additional simulations by incorporating the closure models for $\vec{F}_{GL}$, $\vec{F}_{GS}$, $\vec{F}_{LS}$, $\vec{F}_{D,G}$ and $\vec{F}_{D,L}$ in gas and liquid momentum equations. The closure model for $\vec{F}_C$ was not incorporated and the Q_G, Q_L and fluid physical properties were kept constant. **Figure 3 [(a)-(c)]** shows the effect of d_P on the steady-state liquid volume fraction, and **Figure 3 (d)** shows the comparison of the steady-state liquid fronts for different values of d_P. It can be seen from the **Figure 3 [(a)-(c)]** that the decrease in d_P increases the liquid accumulation, specifically in the center. Also, the spreading was found to increase only near bed inlet and as a result the lateral spreading for $d_P = 2$ mm was found to be of same order at both the inlet and outlet (see **Figure 3 [(a)-(c)])**. This is also evident from the steady-state liquid fronts shown in **Figure 3 (d)**. Thus, $\vec{F}_{D,G}$ and $\vec{F}_{D,L}$ were found to marginally increase the lateral liquid spreading with the decrease in d_P. Furthermore, in order to quantify the increase in $\vec{F}_{D,G}$ and $\vec{F}_{D,L}$ with decrease in d_P, the order of magnitude of different components of $\vec{F}_{D,G}$ and $\vec{F}_{D,L}$ were calculated. The order of magnitude of $F_{D,L,x}$ was found to be significantly higher than that of the $F_{D,L,y}$, $F_{D,G,x}$ and $F_{D,G,y}$ **(Supplementary Figure 3 (a)).** Therefore, only the $F_{D,L,x}$ for different d_P was further compared. It can be seen from the comparison of $F_{D,L,x}$ shown in **Supplementary Figure 3 (b)** that, with the increase in d_P from 2 to 8 mm the contribution of $F_{D,L,x}$ decreases only marginally. Therefore, since the $\vec{F}_{D,G}$ and $\vec{F}_{D,L}$ was found to marginally affect the lateral liquid spreading, in particularly only near the bed inlet, the $\vec{F}_{D,G}$ and $\vec{F}_{D,L}$ forces were not considered in further simulations.

4.2 Contribution of interphase interaction forces at varying gas flow rates

As mentioned in Section 1, that the CFD models reported in literature were not able to accurately predict the effect of Q_G on the local liquid distribution, accurately (e.g., see Solomenko et al., 2015 and Jindal and Buwa, 2017). In order to improve the agreement between the predictions and the corresponding measurements of $\langle \varepsilon_L \rangle$ and $\Delta P/L$, the closure model for $\vec{F}_{LS}$ (proposed by Attou et al., 1999) was empirically modified by Boyer et al. (2007) by introducing an additional factor $(\varepsilon_L/1-\varepsilon_S)^n$ (see **Eqn. (18)**), where the value of exponent 'n' was considered as -0.54 for aqueous fluids and -0.02 for organic fluids.

$$\vec{F}_{LS} = \left(\frac{\varepsilon_L}{1-\varepsilon_S}\right)^n \left(\frac{E_1 \mu_L \varepsilon_S{}^2}{d_P{}^2 \varepsilon_L} + \frac{E_2 \rho_L \varepsilon_S}{d_P} |\vec{u}_L|\right) \vec{u}_L \tag{18}$$

We performed further simulations by incorporating the correction to $\vec{F}_{LS}$ proposed by Boyer et al. (2007) with $n = -0.54$. **Figure 4** shows the steady-state liquid fronts predicted by using the corrected $\vec{F}_{LS}$ with n = -0.54, 0 and 0.45, at different Q_G. It can be seen from **Figure 4[(a)-(c)]** that the agreement between the measured and predicted steady-state liquid spreading was marginally improved at n = 0.45 (specifically at large Q_G).

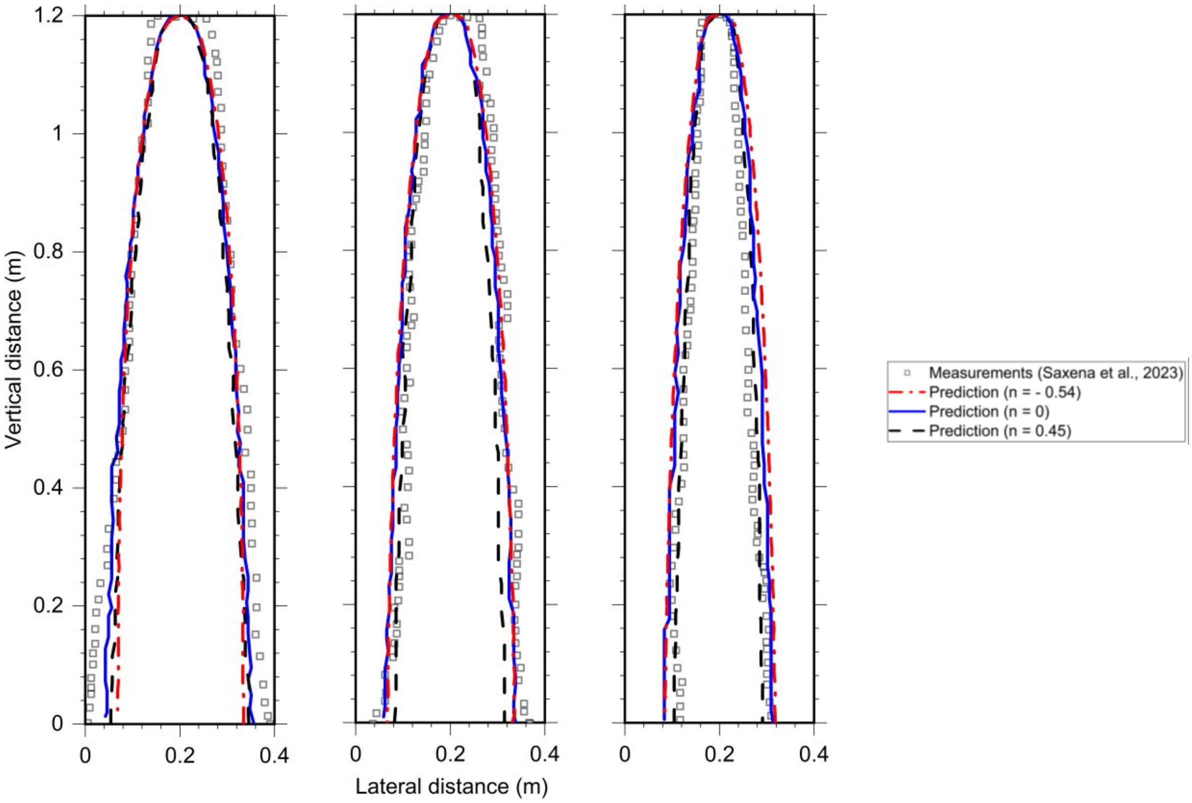

(i) $Q_G = 0$ Nm^3/h (ii) $Q_G = 6$ Nm^3/h (iii) $Q_G = 12$ Nm^3/h

Figure 4. Effect of correction factor "n" on the steady-state liquid fronts at a Q_G of (i) 0, (ii) 6, and (iii) 12, ($Q_L = 0.054$ m^3/h, $d_P = 0.004$ m)

Since the steady-state liquid spreading was found to be marginally influenced by the correction factor "n", the effect of correction factor "n" on the macroscopic key hydrodynamic parameters like $\langle \varepsilon_L \rangle$ and $\Delta P/L$ was investigated. **Figure 5** shows the effect of correction factor "n" on the steady state $\langle \varepsilon_L \rangle$ and $\Delta P/L$ at different Q_G and the comparison of predictions at different "n" with corresponding measurements at different Q_G. Both $\langle \varepsilon_L \rangle$ and $\Delta P/L$ were found to increase with the decrease in "n" from 0 to -0.54, thereby, the agreement between measured and predicted $\langle \varepsilon_L \rangle$ and $\Delta P/L$ was found to deteriorate. Therefore, we investigated the effect of the value of "n", and found that an increase in "n" from 0 to 0.45 led to a significant improvement in the agreement between the predictions and corresponding measurements was found to improve significantly for both $\langle \varepsilon_L \rangle$ and $\Delta P/L$ at a Q_G of 6 and 12 Nm^3/h. Further it can also be seen from the **Supplementary Figure 5 [(a)-(c)]** that on decreasing "n" from 0 to -0.54, the effect of Q_G on the lateral liquid spreading is found to be diminished, whereas on increasing "n" from 0 to 0.45, the model is found to be more sensitive towards the change in Q_G.

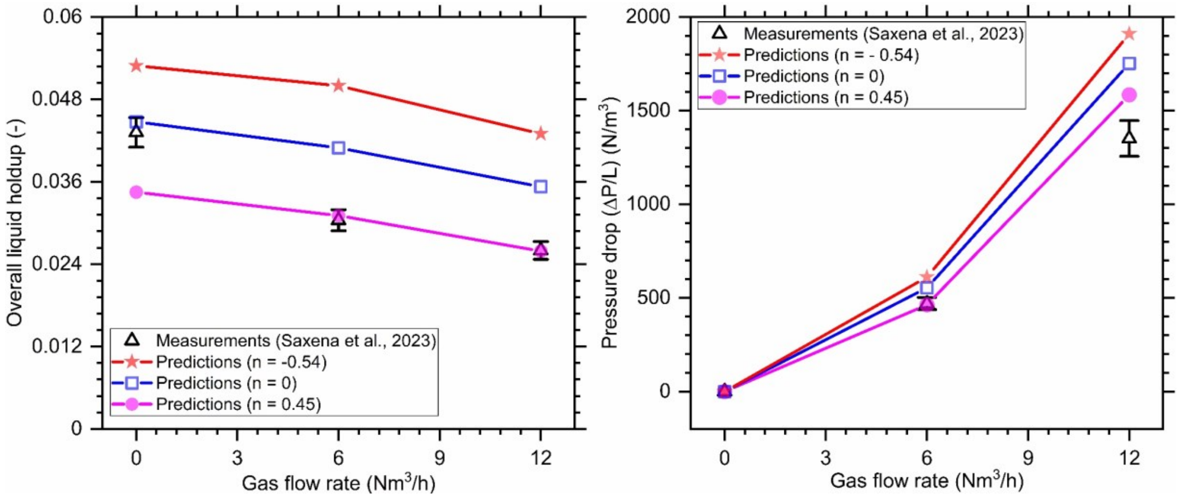

(i) (ii)

Figure 5. Effect of exponent 'n' on (a) overall liquid holdup, (b) pressure drop, at a Q_G of (i) 0 Nm^3/h, (b) 6 Nm^3/h, and (c) 12 Nm^3/h ($Q_L = 0.054\ m^3/h$, $d_P = 0.004$ m)

In order to understand the effect of "n" on the bed scale hydrodynamics, we analysed the order of magnitude of different forces ($F_{GL,y}$, $F_{GS,y}$, $F_{LS,y}$). **Figure 6** shows the histograms of $F_{GL,y}$, $\vec{F}_{GS,y}$, $\vec{F}_{LS,y}$ as well as the volume-weighted-average force (calculated with help of **Eqn. 19)** in the complete domain at steady state conditions.

$$\text{Volume weighted average force (N/m}^3\text{)} = \left(\frac{\sum_{i=1}^{n}(V_i \times |F_{xx,i,y}|)}{V_{total}}\right) \qquad (19)$$

In **Eqn. 19** V_i is the cell volume, $|F_{xx,i,y}|$ is the magnitude of y-component of the respective force, V_{total} is the total bed volume. With the decrease in "n" from 0 to -0.54 a significant increase in the magnitude of $F_{LS,y}$ was predicted (see **Figure 6(a-i) - 6(a-iii))**, whereas the magnitude of $F_{LS,y}$ was found to decrease with the increase in "n" from 0 to 0.45 at all values of Q_G. Since the additional factor of $(\varepsilon_L/1-\varepsilon_S)^n$ was added only in the closure model of $\vec{F}_{LS}$, the changes in $F_{GL,\,y}$ (see **Figure 6(b-i) - 6(b-iii))** and $F_{GS,\,y}$ (see **Figure 6(c-i) - 6(c-iii))** with the change in "n", were found to be marginal and relatively smaller. For n = 0.45 with the increase in Q_G from 0 to 12 Nm^3/h the magnitude of $F_{LS,\,y}$, $F_{GL,\,y}$ and $F_{GS,\,y}$ was found to increase significantly [see **Figures 6(a), 6(b), and 6(c)**]. Since only the Q_G is changed, the predicted increase in the $F_{LS,\,y}$ [see **Figure 6(a-i) – 6(a-iii)**] with the increase in Q_G was secondary and relatively smaller in comparison to that of the predicted increase in the $F_{GL,\,y}$ [see **Figure 6(b-i) – 6(b-iii)**] and $F_{GS,\,y}$ [see **Figure 6(c-i) – 6(c-iii)**]. This also signifies that the gas phase inertia plays an important role in the local liquid distribution at bed-scale.

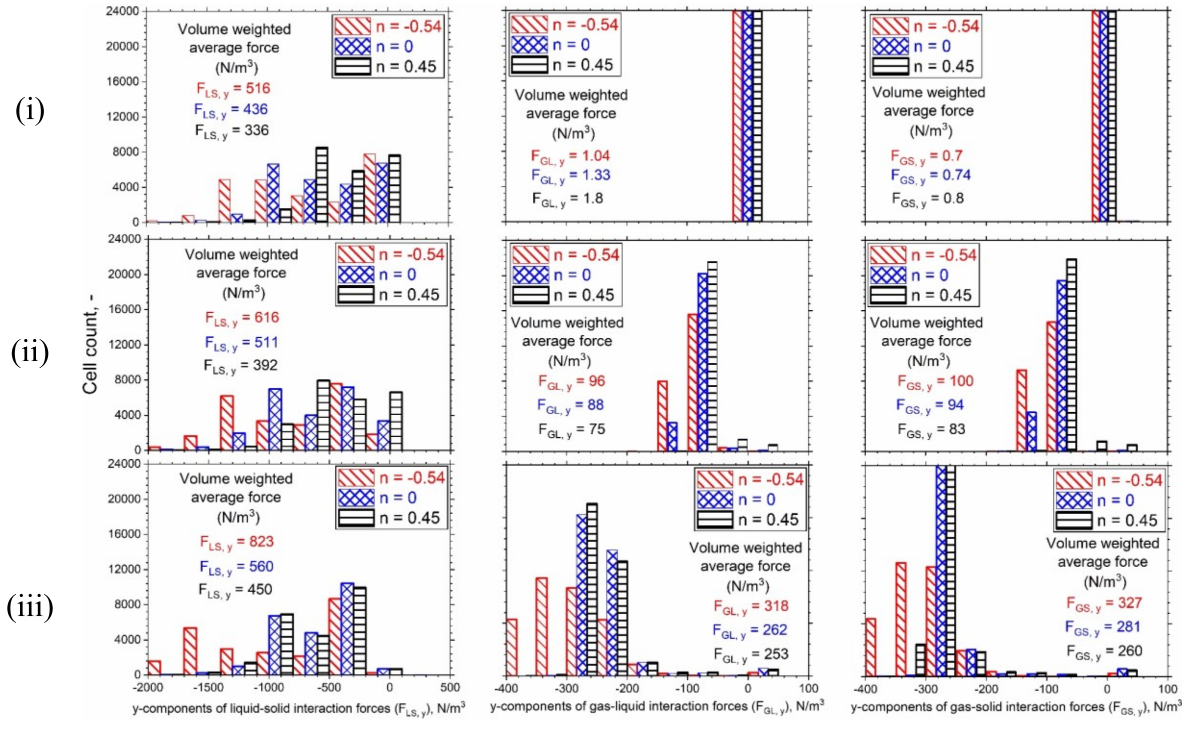

(a) (b) (c)

Figure 6. Effect of correction factor "n" on the magnitude of y-components of different forces, (a) $F_{LS,\,y}$, (b) $F_{GL,\,y}$, and (c) $F_{GS,\,y}$, at Q_G of (i) 0, (ii) 6, and (iii) 12 Nm^3/h (Q_L = 0.054 m^3/h, d_P = 0.004 m)

Figure 7 [(a)-(c)] shows the predicted steady state liquid volume fraction distribution at Q_G of 0, 6 and 12 Nm^3/h, respectively, whereas **figure 7 [(d) and (e)]** shows the measured and predicted steady state liquid fronts, respectively, at Q_G of 0, 6 and 12 Nm^3/h for $n = 0.45$. The agreement between the measured and predicted steady-state liquid fronts is found to be satisfactory (see **Figure 7 [(a)-(c)]**). The lateral liquid spreading was found to decrease with the increase in Q_G from 0 to 12 Nm^3/h. This is due to a significant increase in the magnitude of $F_{GL,\,y}$ and $F_{GS,\,y}$ with the increase in Q_G. Also, due to the increase in the gas-phase inertia, the liquid inside the interstitial capillaries is pushed out with relatively higher force. This decreases the saturation inside these capillaries and as a result the $\langle \varepsilon_L \rangle$ was found to decrease. Hence, a decrease in the lateral liquid spreading with the increase in Q_G is observed in both the measurements and simulations.

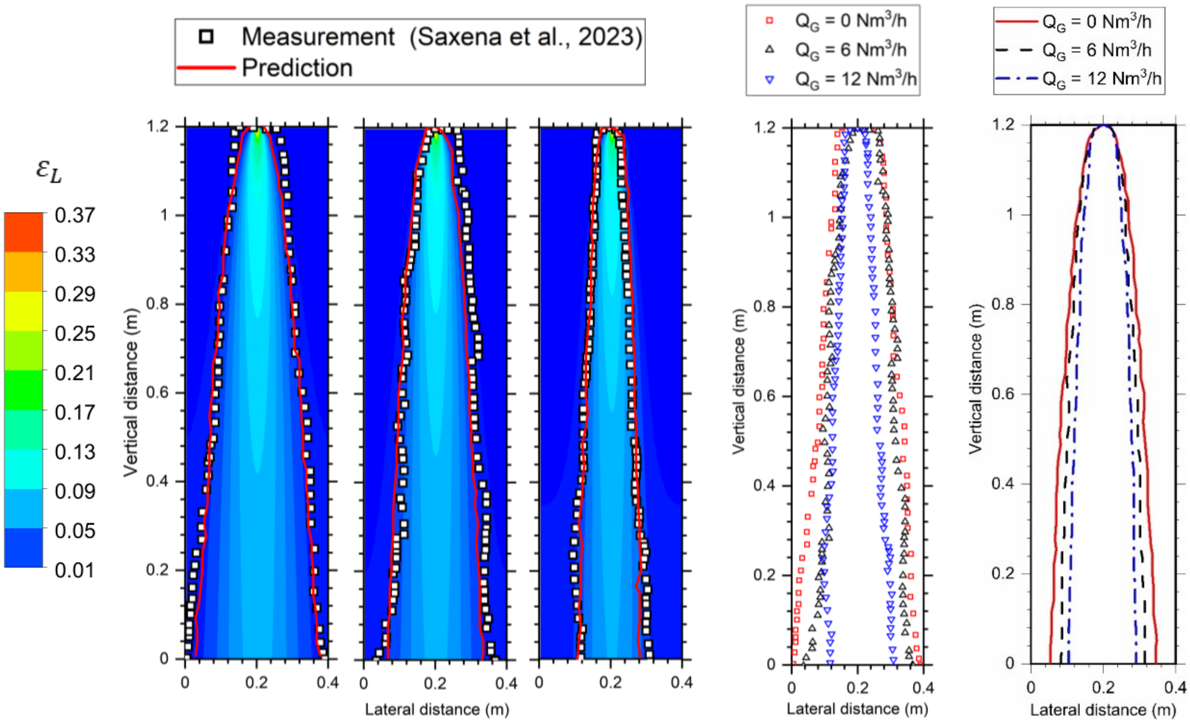

(a) (b) (c) (d) (e)

Figure 7. Effect of gas flow rates on the steady-state liquid distribution at Q_G of (a) 0, (b) 6, and (c) 12 Nm^3/h, and comparison of the (d) measured (Saxena et al., 2023), and (e) predicted steady-state liquid fronts ($Q_L = 0.054$ m^3/h, $d_P = 0.004$ m, $n = 0.45$)

4.3 Effect of liquid flow rate

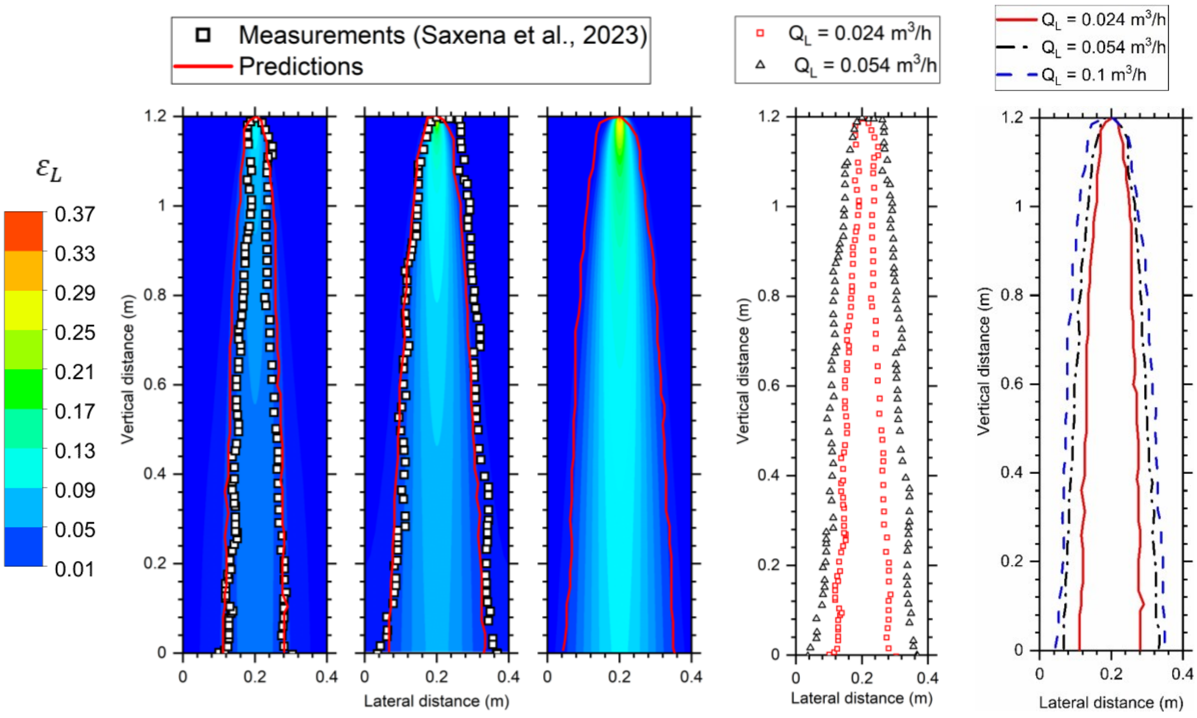

(a) (b) (c) (d) (e)

Figure 8. Effect of liquid flow rates on the steady-state liquid distribution at a Q_L of (a) 0.024, (b) 0.054, and (c) 0.1 m^3/h, and comparison of the (d) measured (Saxena et al., 2023), and (e) predicted steady-state liquid fronts (Q_G = 6 Nm^3/h, d_P = 0.004 m, n = 0.45)

Simulations at three different values of Q_L were performed by keeping the Q_G and bed characteristics constant. **Figure 8 [(a) to (c)]** shows the steady-state liquid volume fraction distribution at Q_L of 0.024, 0.054 and 0.1 m^3/h, respectively. **Figure 8 [(d) and (e)]** shows the measured (Q_L = 0.024 and 0.054 m^3/h) and predicted (Q_L = 0.024, 0.054 and 0.1 m^3/h) steady-state liquid fronts, respectively. The agreement between the measured and predicted steady-state liquid fronts is found to be satisfactory (see **Figure 8 [(a) and (b)]**). In both the measurements and predictions, it was observed that the increase in Q_L promotes the lateral liquid spreading (e.g., see **Figure 7 [(d) and (e)]**). Further, the steady-state liquid volume fraction distribution in **Figure 7 [(a) to (c)]** shows that the liquid accumulation in the center increases with the increase in Q_L. Therefore, the interstitial capillaries are relatively more saturated at large values of Q_L, resulting in an increase in the contribution of gradient of lateral liquid hold-up to the capillary pressure force ($F_{c,x}$) as shown in **Supplementary Figure 6.** Due to this, an increase in lateral liquid spreading is observed in the predictions.

Moreover, the predictions are also validated using the measurements (Saxena et al., 2023) of $\Delta P/L$ and $\langle \varepsilon_L \rangle$ at Q_L of 0.024 and 0.054 m^3/h (see **Figure 9).** The agreement between the predictions and the corresponding measurements is found to be satisfactory. Both $\Delta P/L$ and $\langle \varepsilon_L \rangle$ are found to increase with an increase in Q_L. However, the increase in $\Delta P/L$ was found to be less significant than the increase in $\langle \varepsilon_L \rangle$. Since at large Q_L, increased volume of liquid enters the available pore space, interstitial capillaries are relatively more saturated, and this results in an increase in $\langle \varepsilon_L \rangle$. Thus, relatively higher force is required to push the liquid out from the relatively more saturated capillaries and therefore an increase in $\Delta P/L$ is observed.

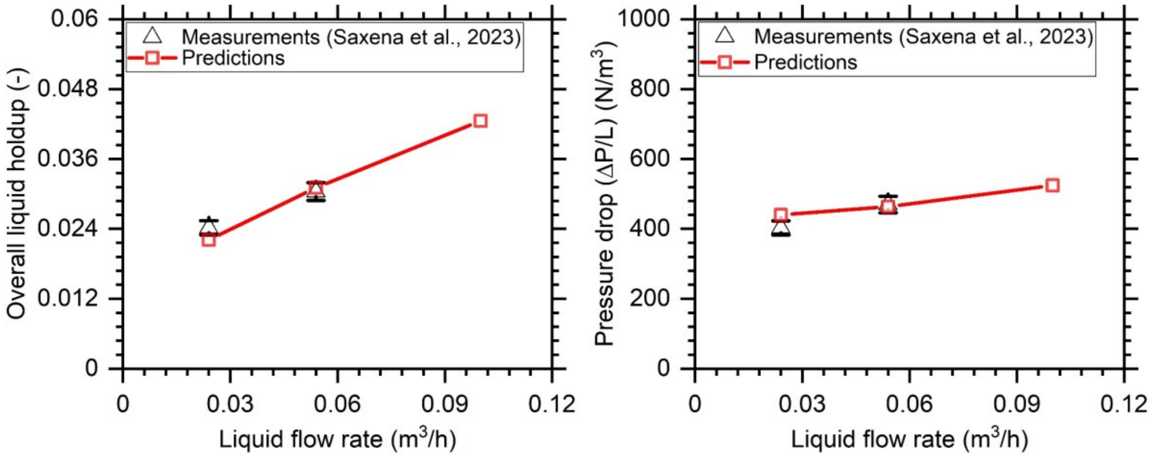

(a) (b)

Figure 9. Effect of liquid flow rates on the (a) overall liquid holdup, and (b) pressure drop. ($Q_G = 6$ Nm^3/h, $d_P = 0.004$ m, $n = 0.45$)

Further, to understand the effect of Q_L, the volume weighted average (calculated using **Eqn. 19**) of $F_{GL,y}$, $F_{GS,y}$, $F_{LS,y}$ was calculated in the complete domain. **Figure 10** shows the change in the distribution and the magnitude of different forces in the complete domain with varying Q_L. Since only the Q_L is changed, the distribution and magnitude of $F_{GL,y}$ and $F_{GS,y}$ is found to increase marginally with the increase in Q_L. Whereas the increase in the magnitude of

$F_{LS,\ y}$ with the increase in Q_L from 0.024 to 0.1 m^3/h was found to be nearly 2.5 times (**e.g., see Figure 10 (c)**).

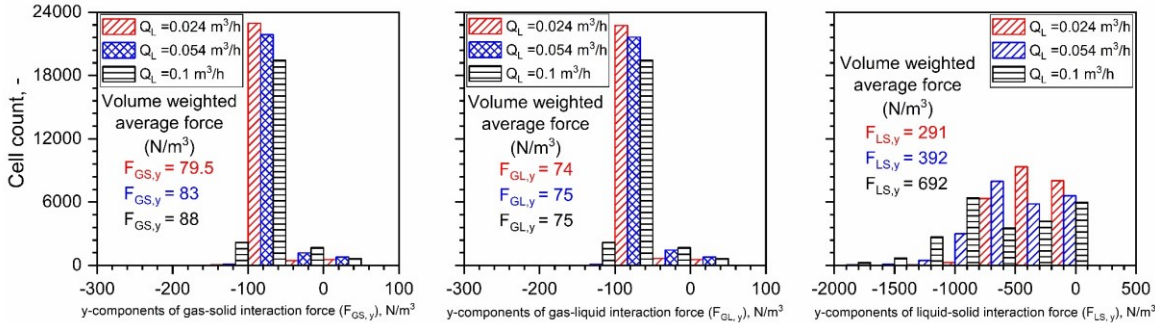

(a) (b) (c)

Figure 10. Effect of the liquid flow rates on the magnitude of the y-components of (a) gas-solid ($F_{GS,\ y}$), (b) gas-liquid ($F_{GL,\ y}$), and (c) liquid-solid ($F_{LS,\ y}$) interphase interaction forces (Q_G = 6 Nm^3/h, d_P = 0.004 m, n = 0.45)

4.4 Effect of surface tension

As discussed in the Section 1, the effect of surface tension on the local liquid distribution at bed-scale using Eulerian multi-fluid model is not investigated earlier. Since different fluids (e.g., aqueous, organic etc.) are usually processed using TBRs, it is important to investigate the effect of σ on the local liquid distribution and on the key hydrodynamic parameters like ΔP/L and $\langle \varepsilon_L \rangle$. In view of this, bed-scale 3D transient simulations are performed for three different values of σ (i.e., 0.025, 0.052 and 0.072 N/m). In all these simulations, the bed characteristics, fluid flow rates and fluid flow properties other than σ are kept constant. **Figure 11** shows the steady-state liquid volume fraction distribution and liquid fronts at the above-mentioned values of σ and the comparison between the predictions and corresponding measurements (Saxena et al., 2023). The agreement between the measured and predicted liquid fronts was found to be satisfactory. The increase in surface tension is found to marginally increase the lateral liquid spreading.

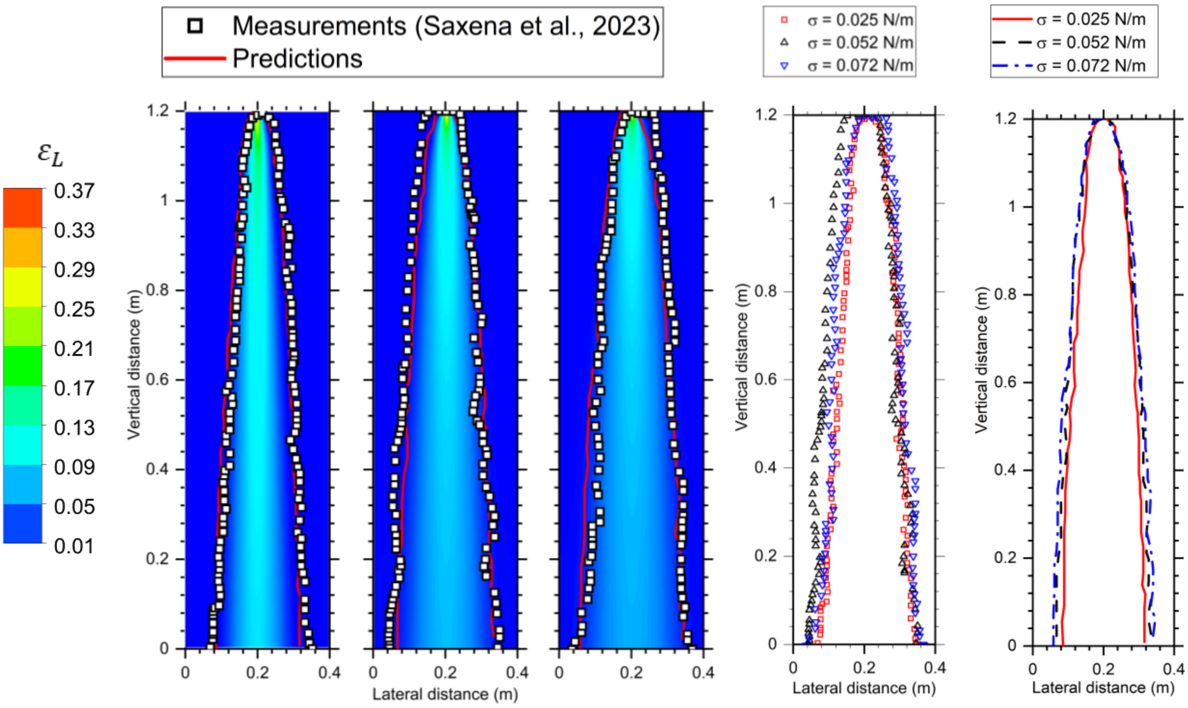

(a) (b) (c) (d) (e)

Figure 11. Effect of σ on the steady-state liquid distribution at σ of (a) 0.025, (b) 0.052, and (c) 0.072 N/m, and comparison of the steady-state (d) measured (Saxena et al., 2023), and (e) predicted liquid fronts (Q_L = 0.054 m^3/h, Q_G = 6 Nm^3/h, d_P = 0.004 m, n = 0.45)

As seen from the capillary pressure model [**see Eqs. (11)-(13)**], $\vec{F}_c$ is directly proportional to the σ and $\Delta\varepsilon_L$. Therefore, liquid spreading is primarily governed by the relative order of magnitude of σ and $\Delta\varepsilon_L$. **Figure 12** shows the change in the liquid volume fraction, $\Delta\varepsilon_L$ and the $F_{c,x}$ at different axial locations at mid plane (i.e., z = 0.01 m). It is found that a decrease in σ leads to an increase in the volume fraction and $\Delta\varepsilon_L$ in the central region. However, irrespective of the increase in $\Delta\varepsilon_L$ with the decrease in σ in the central region, the $F_{c,x}$ is found to decrease. Since the increase in $\Delta\varepsilon_L$ in the central region is not significant to counter the effect of σ on the $F_{c,\ x}$, the lateral liquid spreading is found to marginally decrease with the decrease in σ.

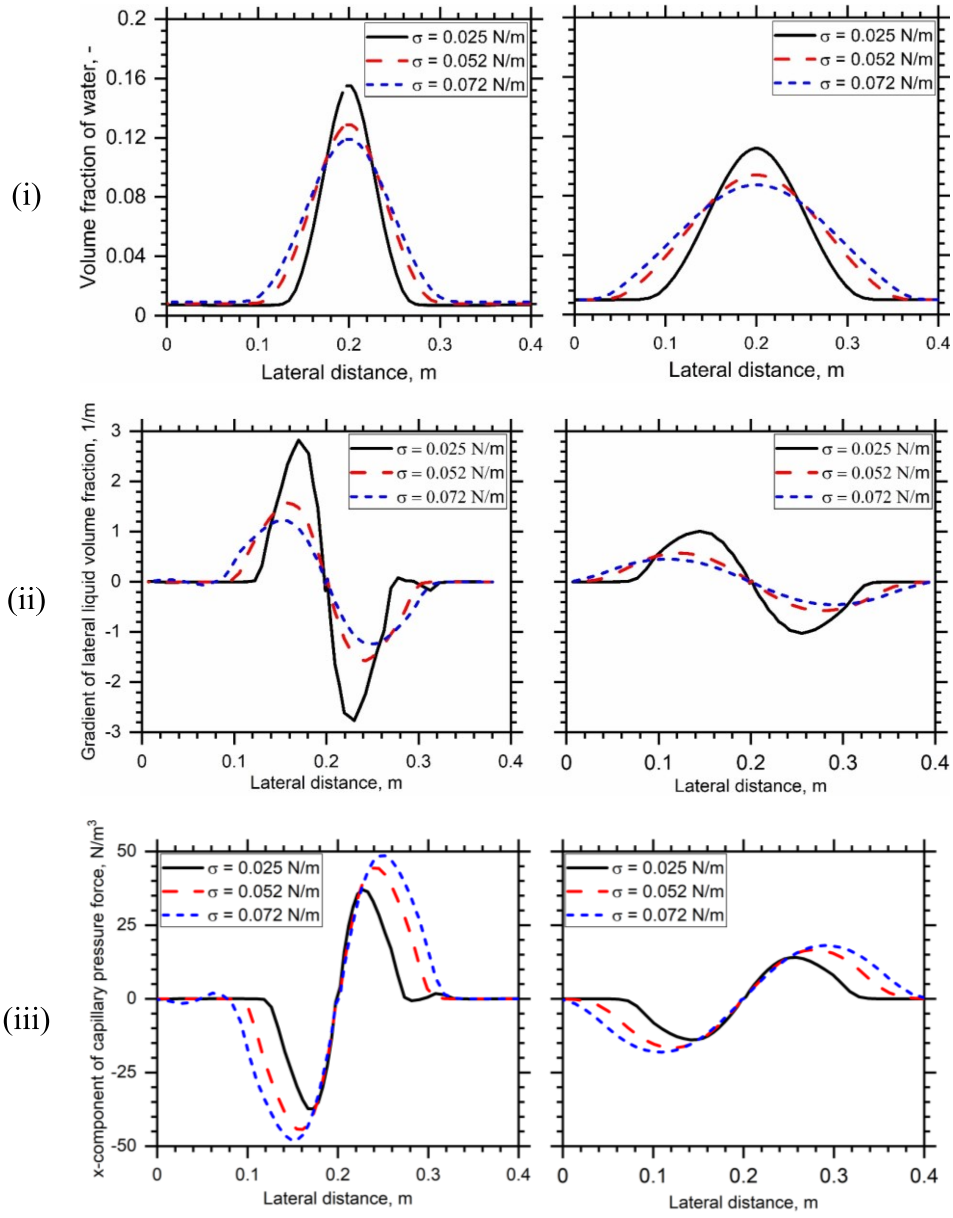

(a) (b)

Figure 12. Effect of surface tension on the (i) volume fraction of water, (ii) gradient of lateral (x-direction) liquid volume fraction, and (iii) x-components of capillary pressure force at the axial locations of (a) Y = 0.1 m, and (b) Y = 0.9 m on the mid plane (i.e., z = 0.01 m) ($Q_L = 0.054\ m^3/h$, $Q_G = 6\ Nm^3/h$, $d_P = 0.004$ m, n = 0.45).

Furthermore, the predictions are also validated with the corresponding measurements of the ΔP/L and $\langle \varepsilon_L \rangle$ (see **Figure 13**). The agreement between the predictions and corresponding measurements was found to be satisfactory. Both ΔP/L and $\langle \varepsilon_L \rangle$ are found to increase with the increase in σ. It can be seen from **Figure 13 (a)** that irrespective of the high liquid accumulation in central region at low σ, $\langle \varepsilon_L \rangle$ is found to be less. This signifies that, at higher σ, the liquid disperses more uniformly in the bed, while at lower σ liquid accumulates more in the central region.

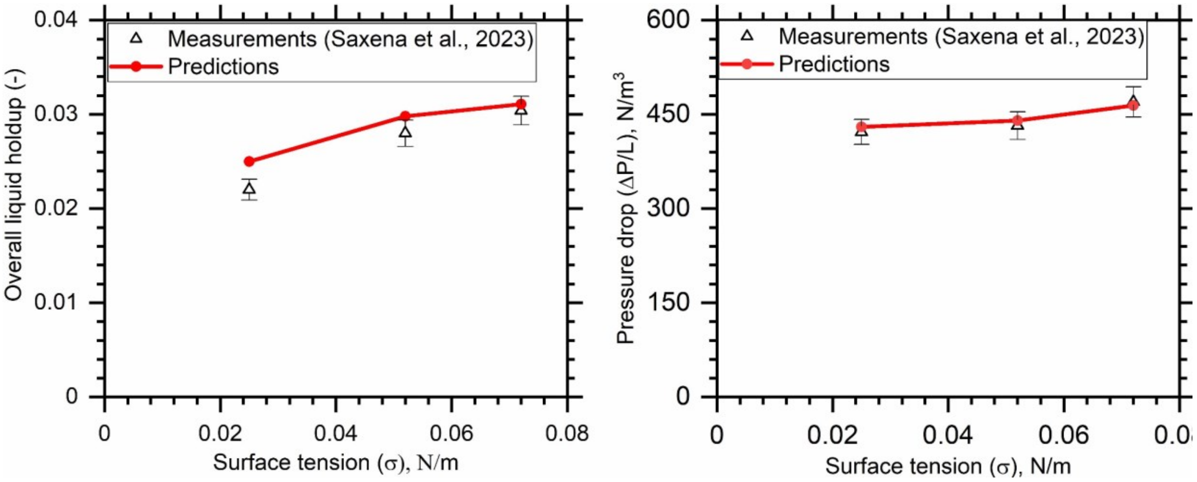

(a) (b)

Figure 13. Effect of surface tension on (a) overall liquid volume fraction, and (b) pressure drop (Q_L = 0.054 m^3/h, Q_G = 6 Nm^3/h, d_P = 0.004 m)

4.5 Effect of liquid viscosity

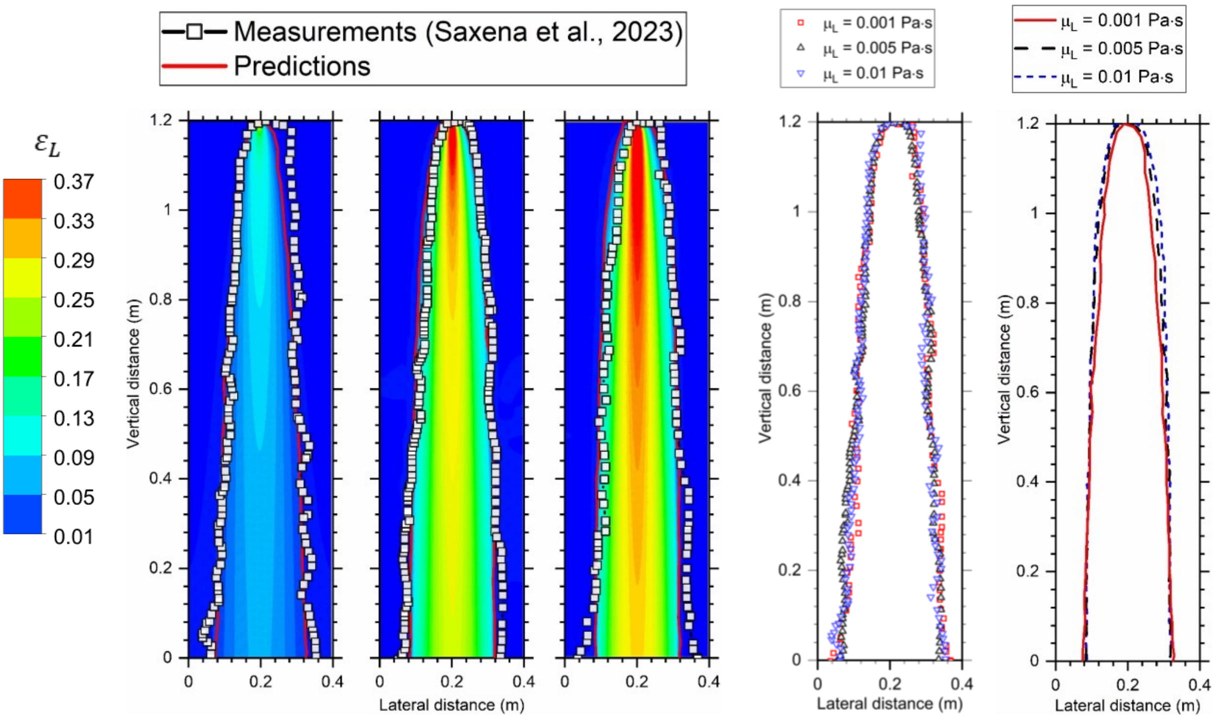

(a) (b) (c) (d) (e)

Figure 14. Effect of liquid viscosity on liquid volume fraction distribution, (a) μ_L = 0.001 Pa·s, (b) μ_L = 0.005 Pa·s, (c) Q_L = 0.01 Pa·s, and comparison of the steady state (d) measured (Saxena et al., 2023), and (e) predicted liquid fronts (Q_L = 0.054 m^3/h, Q_G = 6 Nm^3/h, d_P = 0.004 m)

A discussed in the Section 2, 3D transient bed-scale simulations for three different liquid viscosities (μ_L = 0.001, 0.005 and 0.01 Pa·s) are performed for constant bed characteristics, fluid flow rates, σ and all other parameters. **Figure 14 [(a)-(c)]** shows the steady-state liquid volume fraction distribution and the comparison of the measured and predicted steady-state liquid fronts for μ_L of 0.001, 0.005 and 0.01 Pa·s, respectively. **Figure 14 [(d) and (e)]** shows the effect of μ_L on the measured and predicted steady-state liquid fronts, respectively. The agreement between the measured and predicted steady-state liquid fronts was found to be satisfactory. Further, it can be seen from **Figure 14 [(d) and (e)]** that the extent of liquid spreading is not found to be influenced by the change in μ_L in both the measurements as well as in the simulations. Only a marginal change in the lateral liquid spreading near the bed inlet is observed. Moreover, irrespective of a significant change in local ε_L, which is evident from the liquid volume fraction distribution, the liquid spreading was not found to increase.

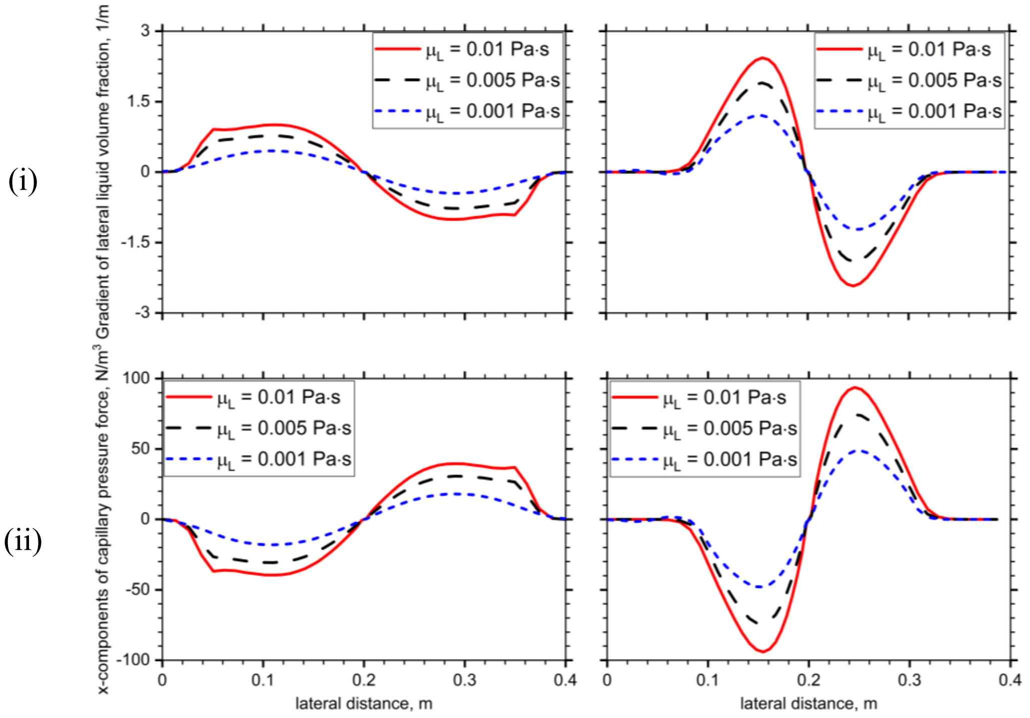

(a) (b)

Figure 15. Effect of liquid viscosities on the (i) gradient of lateral liquid volume fraction, (ii) x-component of capillary pressure force ($F_{c,x}$), at the axial locations of (a) Y = 0.1 m, and (b) Y = 0.9 m on the mid plane (i.e., Z = 0.01 m) (Q_L = 0.054 m^3/h, Q_G = 6 Nm^3/h, d_P = 0.004 m, n = 0.45).

Figure 15 shows that the effect of liquid viscosities on the gradient of lateral liquid volume fraction ($\Delta\varepsilon_L$) and the x-component of capillary pressure force ($F_{C,x}$) at two different locations in the flow direction (Y = 0.1 and 0.9 m). Both $\Delta\varepsilon_L$ and $F_{C,x}$ is found to increase with the increase in μ_L. However, irrespective of the increase in $\Delta\varepsilon_L$ and $F_{C,x}$ with the increase in μ_L, the lateral liquid spreading is not found to change significantly.

The predicted ΔP/L is also validated with the corresponding measurements (Saxena et al., 2023) of the ΔP/L (see **Figure 16**). The agreement between the predictions and measurements is found to be satisfactory. The ΔP/L is found to increase with the increase in μ_L. Due to increase in μ_L, the liquid accumulation in the bed increases and in turn the interstitial capillaries are relatively more saturated at large μ_L. Therefore, relatively a higher force is required to flush out the highly viscous liquid from these interstitial capillaries. This leads to a significant increase in ΔP/L with increase in μ_L, whereas the change in the lateral liquid spreading is negligible.

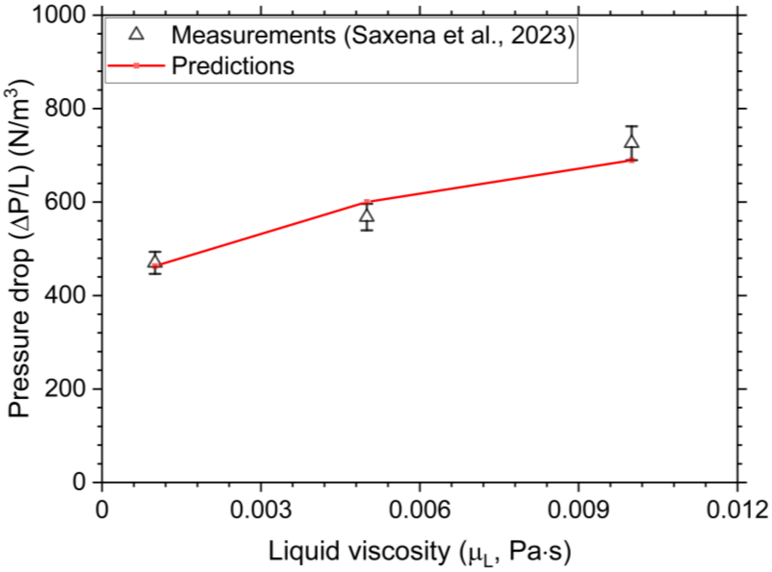

Figure 16. Effect of μ_L on the measured and simulated pressure drop (ΔP/L)

As mentioned in the Section 2, that the closure models for the interphase interaction forces contain the viscous and inertial components of respective forces. **Figure 17 [(a)-(c)]** shows the distribution and the magnitude of the ratios of the y-components of the viscous (v) to inertial (i) components of the interphase exchange forces ($\vec{\mathrm{F}}_{\mathrm{GS}}$, $\vec{\mathrm{F}}_{\mathrm{GL}}$ and $\vec{\mathrm{F}}_{\mathrm{LS}}$). Since only the μ_L is varied, the changes in the predicted $\mathrm{F}_{\mathrm{GS,y,v}}/\mathrm{F}_{\mathrm{GS,y,i}}$ and $\mathrm{F}_{\mathrm{GL,y,v}}/\mathrm{F}_{\mathrm{GL,y,i}}$ are not significant. Due to the increase in μ_L (nearly 10 times), the contribution of $\mathrm{F}_{\mathrm{LS,y,v}}$ increases significantly and leads to a significant increase in $\mathrm{F}_{\mathrm{LS,y,v}}/\mathrm{F}_{\mathrm{LS,y,i}}$ with the increase in μ_L. However, the change in lateral liquid spreading due to the change in $\mathrm{F}_{\mathrm{LS,y,v}}$ is found to be negligible. Therefore, the contribution of the viscous components of the interphase exchange forces to the lateral liquid spreading is found to be negligible.

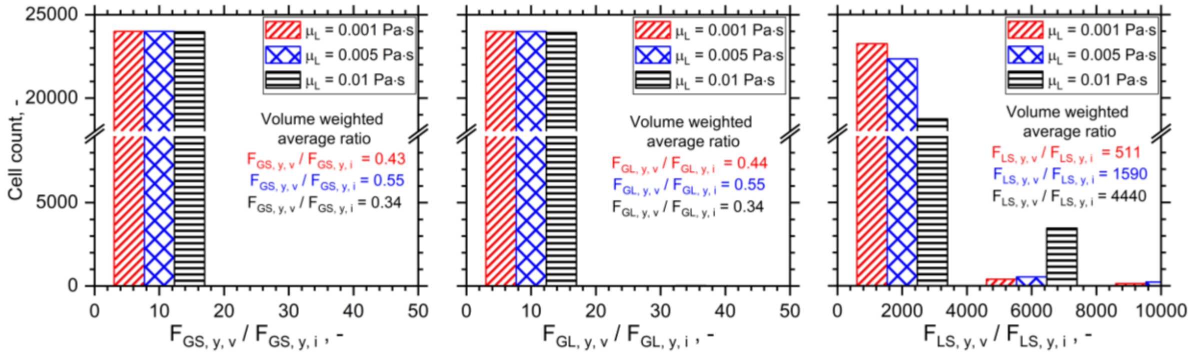

(i) (ii) (iii)

Figure 17. Effect of the μ_L on the ratios of the y-components of the viscous to inertial force components of (i) gas-solid, (ii) gas-liquid, and (iii) liquid-solid interphase interaction forces ($Q_L = 0.054$ m^3/h, $Q_G = 6$ Nm^3/h, $d_P = 0.004$ m, n = 0.45)

5 Summary and conclusions

In the present work, 3D transient Eulerian multi-fluid simulations were performed at different gas ($Q_G = 0$, 6 and 12 Nm^3/h) and liquid flow rates ($Q_L = 0.024$, 0.054 and 0.1 m^3/h), particle diameters ($d_P = 2$, 4 and 8 mm), liquid viscosities ($\mu_L = 0.001$, 0.005 and 0.01 Pa·s), and surface tensions (σ = 0.025, 0.052 and 0.072 N/m). We found that the y-component of the interphase coupling forces ($\mathrm{F}_{\mathrm{GL,y}}$, $\mathrm{F}_{\mathrm{GS,y}}$ and $\mathrm{F}_{\mathrm{LS,y}}$) and the x-component of the mechanical and capillary dispersion forces ($\mathrm{F}_{\mathrm{D,L,x}}$ and $\mathrm{F}_{\mathrm{C,x}}$) are dominating and their contribution to local liquid spreading, ΔP/L and $\langle \varepsilon_\mathrm{L} \rangle$ was analysed. First, the contribution of $F_{D,L,x}$ to the lateral liquid spreading was investigated for d_P of 2, 4 and 8 mm. We found the lateral liquid spreading to marginally increase near to the bed inlet with the decrease in d_P. Further, a satisfactory agreement between the measured and predicted liquid fronts without inclusion of $\vec{F}_{D,L,x}$ suggests that the mechanical dispersion force has a marginal contribution to the local liquid spreading at bed-scale.

Since the model was found to overpredict the ΔP/L and $\langle\varepsilon_L\rangle$, we used the modified closure model for $\vec{F}_{LS}$ proposed by Boyer et al. (2007). However, both the ΔP/L and $\langle\varepsilon_L\rangle$ were found to be the strong function of factor "n" in the additional factor $(\varepsilon_L/1-\varepsilon_S)^n$ included by the Boyer et al. (2007) in the closure model of $\vec{F}_{LS}$ originally proposed by Attou et al. (1999). However the value of "n = -0.54" proposed by Boyer at al. (2007) for aqueous did not correctly predict the lateral liquid spreading, ΔP/L and $\langle\varepsilon_L\rangle$. Therefore, we analyzed the effect of "n" on the relevant interphase coupling forces ($F_{GL,y}$, $F_{GS,y}$ and $F_{LS,y}$) and on the liquid spreading, ΔP/L and $\langle\varepsilon_L\rangle$. We found that the modified model (with "n = 0.45") accurately predicted the effect of Q_G, Q_L, σ and μ_L on the lateral liquid spreading, ΔP/L and $\langle\varepsilon_L\rangle$ and the corresponding predictions were in a satisfactory agreement with the measurements of Saxena et al. (2023).

The experimentally-validated CFD model was further used to investigate the effect of Q_G, Q_L, σ and μ_L on the lateral liquid spreading, ΔP/L and $\langle\varepsilon_L\rangle$. While the lateral liquid spreading and $\langle\varepsilon_L\rangle$ were found to decrease with the increase in Q_G, the ΔP/L was found to increase due to a significant increase in $F_{GL,y}$ and $F_{GS,y}$ with the increase in Q_G. Further, a significant increase in $F_{LS,y}$ with the increase in Q_L led to increase the lateral liquid spreading, ΔP/L and $\langle\varepsilon_L\rangle$. The increase in Q_L was also found to increase the liquid accumulation in the centre. Moreover, irrespective of the increase in the gradient of lateral liquid volume fraction and $F_{C,x}$ in the central region with the increase in σ, the lateral liquid spreading, ΔP/L and $\langle\varepsilon_L\rangle$ were found to decrease. While investigating the contribution of viscous force on the lateral liquid spreading and ΔP/L, we found a negligible change in the lateral liquid spreading irrespective of the significant increase in $\Delta P/L$ and ε_L with the increase in μ_L. Further a significant increase in $F_{GS,y,v}/F_{GS,y,i}$, $F_{GL,y,v}/F_{GL,y,i}$ and $F_{LS,y,v}/F_{LS,y,i}$ with the increase in μ_L signifies that the contribution of the viscous components of interphase coupling forces ($F_{GL,y}$, $F_{GS,y}$ and $F_{LS,y}$) to the lateral liquid spreading was negligible.

While the proposed model predicted the effect of Q_G, Q_L, σ and μ_L on the lateral liquid spreading, $\Delta P/L$ and $\langle \varepsilon_L \rangle$ in a satisfactory agreement with the measurements, it needs to be further verified for different types of fluids (i.e., aqueous, and organic). The understanding on the contribution of different forces to the local liquid spreading at different operating conditions will also help in extending the model to simulate the local liquid distribution for shaped particles.

Authors declarations

Conflict of interest

The authors do not have any conflict to disclose.

Acknowledgements

The authors gratefully acknowledge the financial support provided by the IFP Energies Nouvelles and the PADUM hybrid high-performance computing facility of IIT Delhi for computational resources.

Nomenclature

Symbols

$\vec{F}_{GS}$	Gas-solid interphase interaction force, [N/m^3]
$\vec{F}_{LS}$	Liquid-solid interphase interaction force, [N/m^3]
$\vec{F}_{GL}$	Gas-liquid interphase interaction force, [N/m^3]
$\vec{F}_{D,i}$	Mechanical dispersion force exerted on phase i, [N/m^3]
E_1, E_2	Ergun's constant (180 and 1.8, respectively), [-]

P	Pressure, [N/m^2]
ΔP	Pressure drop across bed, [N/m^2]
P_c	Capillary pressure, [N/m^2]
$\vec{F}_C$	Capillary pressure force, [N/m^3]
Q_G	Gas flow rate, [Nm^3/h]
Q_L	Liquid flow rate, [m^3/h]
S_m	Spread factor, [m]
$\vec{u}_i$	Velocity vector of phase i, [m/s]
$\vec{u}_{D,i}$	Drift velocity vector of phase i, [m/s]
d_p	Particle diameter, [m]
d_{thr}	Throat diameter, [m]
L	Length of the column, [m]
“n”	Correction factor, [-]
V_B	Bed volume, [m^3]
V_P	Pore volume, [m^3]

Greek letters

ε_i	Volume fraction of phase i, [-]
ε	Bed void-fraction, [-]
$\langle \varepsilon_L \rangle$	Overall liquid-holdup, [-]
ρ_i	density of phase i, [kg/m^3]
μ_i	viscosity of phase i, [kg/m/s]
σ	Surface tension, [N/m]
π	Constant (3.14), [-]

Subscripts

i = L	liquid
i = G	gas
i = S	solid
x	lateral direction
y	axial direction

z	depth
v	viscous component
i	Inertial component

Acronyms

TBR	Trickle Bed Reactor
CFD	Computational Fluid Dynamics

References

Agrawal, R., West, D.H., Balakotaiah, V., 2007. Modeling and analysis of local hot spot formation in down-flow adiabatic packed-bed reactors. Chem. Eng. Sci. 62, 4926–4943.

Al-Dahhan, M.H., Khadilkar, M.R., Wu, Y., Duduković, M.P., 1998. Prediction of Pressure Drop and Liquid Holdup in High-Pressure Trickle-Bed Reactors. Ind. Eng. Chem. Res. 37, 793–798.

Atta, A., Roy, S., Nigam, K.D.P., 2007. Investigation of liquid maldistribution in trickle-bed reactors using porous media concept in CFD. Chem. Eng. Sci. 62, 7033–7044.

Attou, A., Ferschneider, G., 2000. A two-fluid hydrodynamic model for the transition between trickle and pulse flow in a concurrent gas-liquid packed-bed reactor. Chem. Eng. Sci. 21.

Attou, A., Ferschneider, G., 1999a. A two-fluid model for flow regime transition in gas-liquid trickle-bed reactors. Chem. Eng. Sci. 7.

Attou, A., Ferschneider, G., 1999b. A two-fluid model for flow regime transition in gas-liquid trickle-bed reactors. Chem. Eng. Sci. 7.

Boyer, C., Koudil, A., Chen, P., Dudukovic, M.P., 2005. Study of liquid spreading from a point source in a trickle bed via gamma-ray tomography and CFD simulation. Chem. Eng.

Sci. 60, 6279–6288.

Boyer, C., Volpi, C., Ferschneider, G., 2007. Hydrodynamics of trickle bed reactors at high pressure: Two-phase flow model for pressure drop and liquid holdup, formulation, and experimental validation. Chem. Eng. Sci. 62, 7026–7032.

Dhanraj, D.I.A., Buwa, V.V., 2018. Effect of capillary pressure force on local liquid distribution in a trickle bed. Chem. Eng. Sci. 191, 115–133.

Fourati, M., Roig, V., Raynal, L., 2013. Liquid dispersion in packed columns: Experiments and numerical modeling. Chem. Eng. Sci. 100, 266–278.

Ghanbarian, B., Hunt, A.G., Ewing, R.P., Sahimi, M., 2013. Tortuosity in Porous Media: A Critical Review. Soil Sci. Soc. Am. J. 77, 1461–1477.

Gunjal, P.R., Ranade, V.V., Chaudhari, R.V., 2005. Dynamics of drop impact on solid surface: Experiments and VOF simulations. AIChE J. 51, 59–78.

Gunjal, P.R., Ranade, V.V., Chaudhari, R.V., 2003. Experimental and computational study of liquid drop over flat and spherical surfaces. Catal. Today 79–80, 267–273.

Jiang, Y., Khadilkar, M.R., Al-Dahhan, M.H., Dudukovic, M.P., 2002. CFD of multiphase flow in packed-bed reactors: I.k-Fluid modeling issues. AIChE J. 48, 701–715.

Jindal, A., Buwa, V.V., 2017. Effect of bed characteristics on local liquid spreading in a trickle bed. AIChE J. 63, 347–357.

Lappalainen, K., Gorshkova, E., Manninen, M., Alopaeus, V., 2011. Characteristics of liquid and tracer dispersion in trickle-bed reactors: Effect on CFD modeling and experimental analyses. Comput. Chem. Eng. 35, 41–49.

Lappalainen, K., Manninen, M., Alopaeus, V., 2009a. CFD modeling of radial spreading of flow in trickle-bed reactors due to mechanical and capillary dispersion. Chem. Eng. Sci. 64, 207–218.

Lappalainen, K., Manninen, M., Alopaeus, V., Aittamaa, J., Dodds, J., 2009b. An Analytical

Model for Capillary Pressure–Saturation Relation for Gas–Liquid System in a Packed-Bed of Spherical Particles. Transp. Porous Media 77, 17–40.

Narasimhan, C. S. L., R. P. Verma, Arunabha Kundu, and K. D. P. Nigam. "Modelling hydrodynamics of trickle-bed reactors at high pressure." *AIChE journal* 48, no. 11 (2002): 2459-2474.

R.A. Holub, M.P. Duduković, P.A. Ramachandran. A phenomenological model for pressure drop, liquid holdup, and flow regime transition in gas-liquid trickle flow, Chemical Engineering Science, Volume 47, Issues 9–11, 1992, Pages 2343-2348, ISSN 0009-2509,

Sáez, A.E., Carbonell, R.G., 1985. hydrodynamic parameters for gas-liquid concurrent flow in packed beds. AIChE J. 31, 52–62.

Saxena, D., Gulia, RS., Buwa, V.V., 2023. Experimental characterization of dynamics of liquid spreading in a Trickle bed: Effect of varing fluid flow rates and fluid physical properties. Internal Report, Indian Institute of Technology Delhi, New Delhi.

Solomenko, Z., Haroun, Y., Fourati, M., Larachi, F., Boyer, C., Augier, F., 2015. Liquid spreading in trickle-bed reactors: Experiments and numerical simulations using Eulerian–Eulerian two-fluid approach. Chem. Eng. Sci. 126, 698–710.